



Cite this: *Phys. Chem. Chem. Phys.*,
2015, 17, 12970

First-principles investigation of novel polymorphs of $\text{Mg}_2\text{C}^\dagger$

Changzeng Fan* and Jian Li

On the basis of the evolutionary methodology for crystal structure prediction, the potential crystal structures of magnesium carbide with a chemical composition of Mg_2C are explored. Except the known cubic phase ($Fm\bar{3}m$), two novel tetragonal structures ($P4_2/mnm$ and $I4_1/Amd$) and two novel hexagonal structures ($P6_3/mmc$ and $P\bar{6}M2$) of Mg_2C are found. All these four new phases are mechanically and dynamically stable by the calculated elastic constants and phonon dispersions. Furthermore, the effects of pressure and temperature on the phase transitions among different Mg_2C polymorphs are investigated, implying that some new phases especially the $P4_2/mnm$ phase may be synthesized in future. The ratio values of B/G are also calculated in order to analyze the brittle and ductile nature of these Mg_2C phases. In addition, electronic structure calculations suggest that the $I4_1/Amd$ phase is semimetallic and the other three new phases are all metallic, which is different from the previously proposed magnesium carbides. Meanwhile, the calculated electronic density maps reveal that strong ionic bonding exists between the Mg and C atoms.

Received 1st January 2015,
Accepted 10th April 2015

DOI: 10.1039/c5cp00001g

www.rsc.org/pccp

Introduction

Alkali and alkaline earth metal carbides have received considerable attention from both fundamental and applied perspectives.^{1–4} Among them, the magnesium–carbon system maybe a very promising domain for the discovery of new advanced materials, such as novel polymorphs of “polymeric” carbides with one-dimensional carbon chains,⁵ and Mg-intercalated sp^3 and/or sp^2 carbon networks (clathrates,⁶ doped polymerized fullerenes,⁷ etc.).

The ambient-pressure chemistry of the Mg–C system was investigated quite thoroughly in the past.³ Four magnesium carbides are well known: (1) tetragonal MgC_2 , (2) orthorhombic $\alpha\text{-Mg}_2\text{C}_3$, (3) monoclinic $\beta\text{-Mg}_2\text{C}_3$ and (4) cubic Mg_2C . MgC_2 is a binary carbide with a tetragonal structure⁸ (space group $P4_2/mnm$, no. 136) and originally prepared by Novák in 1910 by the reaction of magnesium and acetylene.⁹ The crystal structure of MgC_2 with C_2^{2-} dumbbells is aligned in the perpendicular direction of the tetragonal c axis. $\alpha\text{-Mg}_2\text{C}_3$ is another Mg–C crystal (space group $pnmm$, no. 58), and a relatively pure product of this compound was obtained with carbon and MgO as impurities by Fjellvag and Karen in 1992.¹⁰ The orthorhombic structure is one of only a handful of examples that contain the rare $[\text{C}=\text{C}=\text{C}]^{4-}$ unit. Very recently, a new monoclinic variation of magnesium sesquicarbide ($\beta\text{-Mg}_2\text{C}_3$) is synthesized from the elements under high-pressure and high-temperature

conditions.¹¹ Like orthorhombic $\alpha\text{-Mg}_2\text{C}_3$, monoclinic $\beta\text{-Mg}_2\text{C}_3$ (space group $C2/m$, no. 12) contains linear $[\text{C}=\text{C}=\text{C}]^{4-}$ chains that are isoelectronic with CO_2 . Mg_2C was hypothesized in 1993 by Corkill and Cohen¹² and obtained by Kurakevych *et al.*^{13,14} under high-pressure conditions very recently. This compound takes on the antifluorite structure (space group $Fm\bar{3}m$, no. 225) with lattice parameter $a = 5.4480 \text{ \AA}$ at ambient pressure and forms from elements at pressure above 15 GPa. Interestingly, it is also fully recoverable to ambient conditions and contains the very unusual C^{4-} anions. Contrary to Mg_2C_3 and MgC_2 , Mg_2C does not contain covalent C–C bonds. Theoretical studies show that Mg_2C is a narrow band gap semiconductor with large elastic modulus.^{15–17} Hence it is promising as a possible material for high pressure and temperature.

In this work, several potential crystal structures of Mg_2C have been predicted by using genetic algorithms. Their stability is determined by elastic constants and phonon spectra. Their transition behaviours under high-pressure and at high-temperature have been extensively investigated. In addition, the mechanical and electronic properties are discussed as well.

Calculation methods

There are several available structure prediction methods for solids.^{18–20} Among these methods, genetic algorithms are well-suited for the task of crystal structure prediction: using “learning” from the history of the simulation, evolution guides search towards low-energy structures; improving the results from generation to generation, such simulations “zoom” in

State Key Laboratory of Metastable Materials Science and Technology, Yanshan University, Qinhuangdao 066004, P. R. China. E-mail: chzfan@ysu.edu.cn

[†] Electronic supplementary information (ESI) available. See DOI: 10.1039/c5cp00001g

on the most promising part of the energy landscape until the lowest-energy structure is found. Several codes All evolutionary simulations were performed with the USPEX code,^{21–23} using VASP for structure relaxation and energy calculation at ambient pressure.²⁴ We performed the searching with up to 7 formula units in the simulation cell and the composition during the search is fixed to Mg₂C. The first generation of structures was created randomly and the number of structures in the population was set to 200. The upper 60% of each generation were used to produce the next-generation structures by heredity. The rest are produced by soft mutation (20%), random space group specificity (10%), and lattice mutation (10%). The best structure of previous generation was set to survive and compete in the following generation. Twenty-five generations (maximum) were required in our global optimisation. There are at least 300 structures have been predicted for each unit-cell composition and more than 2000 structures in total have been explored.

For the selected candidate structures, geometry optimizations and property calculations were implemented in the VASP code, which were carried out using the all-electron projector-augmented wave (PAW) method²⁵ within the framework of density functional theory (DFT).²⁶ The generalized gradient approximation (GGA) in the parameterization of Perdew–Burke–Ernzerhof (PBE) was used as approximation for the exchange and correlation functional.²⁷ The PAW pseudopotentials²⁸ are adopted, with 2p⁶3s² and 2s²2p² electrons were considered as the valence electrons for Mg and C atoms, respectively. Lack of experimental as well as other theoretical results on the investigated system motivated us to perform the present study using different exchange–correlation (XC) schemes. Besides the above mentioned GGA-PBE method, the local density approximation (LDA) has been used, after the work of Ceperley and Alder, using the parametrization given by Perdew and Zunger.^{29,30} In addition, a modified version of the PBE functional which leads to better outcomes for solid systems has also been used (PBESol).³¹ For Brillouin zone integration, we used the Monkhorst–Pack scheme³² and checked convergence of ground state calculations with uniformly increasing *k*-points meshes for each structure. We used a plane-wave basis-set cutoff energy of 480 eV and generated 8 × 8 × 8, 7 × 7 × 10, 10 × 10 × 4, 11 × 11 × 9, and 8 × 8 × 3 *k*-point grids for the *Fm* $\bar{3}$ *m*, *P*₄₂/*mmn*, *P*₆₃/*mmc*, *P* $\bar{6}$ *M*2 and *I*₄₁/*Amd* phases, respectively. In addition, to ensure that the obtained structures are dynamically stable, we calculated phonon frequencies throughout the Brillouin zone using the supercell method in the Phonopy code.³³ The calculation of the elastic constant was carried out using the CASTEP code.³⁴

The temperature–pressure phase diagram has been explored using quasi-harmonic approximation. The Helmholtz energy *F* at volume *V* and temperature *T* can be approximated as

$$F(V, T) = E(V) + F_{\text{vib}}(V, T) \quad (1)$$

Under quasi-harmonic approximation, *F*_{vib}(*V*, *T*) can be calculated from phonon DOS by

$$F_{\text{vib}}(V, T) = Nrk_{\text{B}}T \int_0^\infty d\omega g(\omega, V) \ln \left[2 \sinh \left(\frac{\hbar\omega}{2k_{\text{B}}T} \right) \right] \quad (2)$$

where *F* is the free energy of the primitive unit cell, *N* is the number of primitive unit cells, *r* is the number of degrees of freedom in the primitive unit cells, ω is the phonon frequency, *g*(ω) is the phonon DOS at frequency ω , \hbar is the Planck constant, and *k_B* is Boltzmann's constant. The phonon frequencies were calculated by the supercell approach, which uses the forces obtained by the Hellmann–Feynman theorem calculated from the optimized supercell. Then the Gibbs free energy *G* was calculated from the Helmholtz free energy as

$$G(P, T) = F(V, T) + PV \quad (3)$$

Results and discussion

Structural features

All candidate structures with composition Mg₂C were predicted by the *ab initio* evolutionary structure prediction algorithm. Except the known cubic phase (space group *Fm* $\bar{3}$ *m*, which is an anti-CaF₂ type), four novel dynamical stable AB₂ polymorphs of Mg₂C have been uncovered and selected for further study in this work based on their low enthalpy and high symmetry. The detailed crystallographic data of the known cubic Mg₂C (*Fm* $\bar{3}$ *m* phase) are introduced elsewhere (ref. 13 and 17). The schematic ambient structure of the first new phase is shown in Fig. 1, suggesting a tetragonal system with the space group *P*₄₂/*mmn* (no. 136), which is the well-known Rutile structure and identical to the tetragonal MgC₂ phase. The unit cell is composed of 6 atoms, of which Mg atoms occupy the Wyckoff 4*f* position, while the C atoms take the 2*a* position. In the *P*₄₂/*mmn* phase, every Mg atom is bonded with the nearest 3 C atoms, while every C atom is coordinated by 6 Mg atoms, forming an Mg₆C octahedral. The second new phase also belongs to the tetragonal crystal system and contains 12 atoms in the conventional unit cell (space group *I*₄₁/*Amd*, no. 141, see Fig. 2), which is the well-known Anatase structure. In the *I*₄₁/*Amd* phase, Mg and C atoms occupy Wyckoff 8*e* and 4*a* positions, respectively. Meanwhile, the coordination environment of the phase is similar to the *P*₄₂/*mmn* phase. Mg is 3-coordinate by C atoms and C is octahedrally coordinated by six Mg atoms, see the right side of Fig. 2. Both the third and the forth new phase belong to the hexagonal system, and space group is *P*₆₃/*mmc* (no. 194)

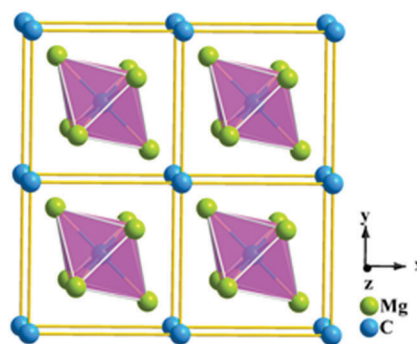


Fig. 1 Schematic image of the *P*₄₂/*mmn* phase. The red polyhedra are drawn to show the coordination environment of C atoms.

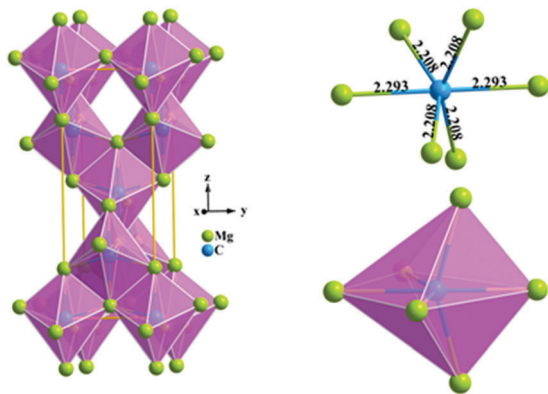


Fig. 2 Schematic image of the $I4_1/Amd$ phase and the coordination environment of C atoms.

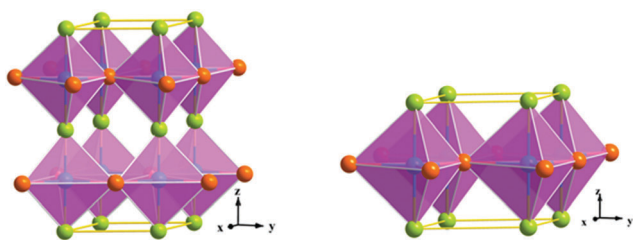


Fig. 3 Schematic image of $P6_3/mmc$ and $P6M2$ phases. Mg1, Mg2 and C atoms are denoted in green, orange and blue, respectively.

and $P6M2$ (no. 187), respectively. In the $P6_3/mmc$ phase, the well-known Molybdenite structure, there are 6 atoms in the unit cell, of which C and two inequivalent Mg (Mg1 and Mg2) atoms occupy $2b$, $2a$ and $2c$ positions, respectively. Each C atom is coordinated by two Mg1 and three Mg2 atoms, forming a Mg_5C triangular pyramid (see Fig. 3), whereas the Mg1 and Mg2 atoms are coordinated by the nearest two and three C atoms, respectively. In the $P6M2$ phase, the unit cell is only composed of 3 atoms. The Mg atoms are split into two categories, Mg1 and Mg2, which take Wyckoff $1a$ and $1f$ positions, respectively, and the C atoms occupy the $1b$ position. In terms of the coordination

environment, these two phases are identical, which is shown in Fig. 3. In the structure, the $P6_3/mmc$ phase can be designated as the double $P6M2$ phase with a similar distance of Mg–C bonds. The detailed optimized crystallographic data of these phases can be found in Table 1. From this table, one can notice that the optimized lattice constants using different exchange–correlation functional are consistent with each other.

Stabilities of new phases

To verify the mechanical stability of these new phases, the elastic stiffness constants of the phases that kept their structures at the ground state after full optimizations were calculated and summarized in Table 2. Because both of these two new phases belong to the tetragonal and hexagonal crystal system, thus there are six and five independent elastic constants, respectively. For the tetragonal (II) crystal (Laue class: $4/m$), the corresponding mechanical stability criterion³⁵ is as follows:

$$C_{11} > |C_{12}|, \quad (C_{11} + C_{12})C_{33} > 2C_{13}^2 \quad (4)$$

$$C_{44} > 0, \quad (C_{11} - C_{12})C_{66} > 2C_{16}^2$$

For the hexagonal crystal system, the mechanical stability can be judged by

$$C_{11} > |C_{12}|, \quad (C_{11} + C_{12})C_{33} > 2C_{13}^2 \quad (5)$$

$$C_{44} > 0, \quad C_{66} > 0$$

According to the criterion and values in Table 2, the newly proposed phases are all mechanically stable at the ground state.

Dynamic stability is also important for a structure, as the appearance of soft phonon modes will lead to the distortion of the crystal. Phonon dispersions in the whole Brillouin zone of the four new phases are plotted in Fig. 4. The inexistence of imaginary frequencies indicates the dynamic stability of the new phases. Therefore, being both mechanically and dynamically stable, these new phases may find some technological applications in future.

Thermodynamic stability has been calculated relative to *hcp* Mg and other 3 phases: MgC_2 (space group $P4_2/mnm$, no. 136), α - Mg_2C_3 (space group $pnmm$, no. 58) and β - Mg_2C_3 (space group $C2/m$, no. 12). The results are summarized in Tables S1–S3 (ESI†).

Table 1 Crystallographic information for various Mg_2C polymorphs at ambient pressure

Structure (space group no.)	Lattice parameter (Å)			Fractional atomic coordinates PBE
	PBE	LDA	PBEsol	
$P4_2/mnm$ (no. 136)	$a = 5.083$ $b = 5.083$ $c = 3.538$	$a = 4.992$ $b = 4.992$ $c = 3.487$	$a = 5.054$ $b = 5.054$ $c = 3.519$	Mg1@4f (0.192, 0.808, 0.500) C1@2a (0.500, 0.500, 0.500)
$I4_1/Amd$ (no. 141)	$a = 4.250$ $b = 4.250$ $c = 11.395$	$a = 4.181$ $b = 4.181$ $c = 11.208$	$a = 4.228$ $b = 4.228$ $c = 11.324$	Mg1@8e (0.000, 0.500, 0.050) C1@4a (0.000, 1.000, 0.000)
$P6_3/mmc$ (no. 194)	$a = 3.894$ $b = 3.894$ $c = 8.416$	$a = 3.822$ $b = 3.822$ $c = 8.295$	$a = 3.863$ $b = 3.863$ $c = 8.386$	Mg1@2a (0.000, 0.000, 0.000) Mg2@2c (−0.333, 0.333, −0.250) C1@2b (0.000, 0.000, 0.750)
$P6M2$ (no. 187)	$a = 3.891$ $b = 3.891$ $c = 4.210$	$a = 3.821$ $b = 3.821$ $c = 4.146$	$a = 3.860$ $b = 3.860$ $c = 4.196$	Mg1@1a (1.000, 0.000, 1.000) Mg2@1f (0.667, 0.333, 0.500) C1@1b (1.000, 0.000, 0.500)

Table 2 The calculated values of elastic constants C_{ij} (GPa), bulk modulus (GPa), shear modulus (GPa) and the B/G ratio of the newly discovered phases. $C_{16} = 0$ for $P4_2/mnm$ and $I4_1/Amd$

Phases	C_{11}	C_{33}	C_{44}	C_{66}	C_{12}	C_{13}	B	G	B/G
$P4_2/mnm$	109.4	200.3	70.4	86.7	72.6	36.8	78.3	54.9	1.43
$I4_1/Amd$	153.0	97.1	8.4	19.8	16.1	39.7	65.4	21.4	3.06
$P6_3/mmc$	76.3	233.7	14.2	9.0	58.4	11.4	58.3	25.8	2.26
$P6M2$	85.5	234.7	14.4	19.2	47.2	12.0	58.5	20.6	2.84

It is also found that the newly proposed Rutile structure is most likely to be synthesized.

The enthalpy curves of the selected structures relative to the $Fm\bar{3}m$ phase as a function of pressure from -10 GPa to 50 GPa are calculated with GGA-PBE functional, as shown in Fig. 5. The effect of “negative pressure” has also been studied as some hypothetical polymorphs have a lower density than the cubic structure and might be stabilized when applying tensile stress.^{36,37} As shown in Fig. 5, the *Rutile* phase (S.G. $P4_2/mnm$) is the most stable structure because it has the lowest enthalpy than those of other phases at relatively lower pressure. When the pressure is higher than approximately 0.8 GPa, the *cubic* phase gets a lower enthalpy than that of the *Anatase* (S.G. $I4_1/Amd$) phase, implying that it is a more stable structure compared with others, as plotted in the inset of Fig. 5. When the pressure is lower than approximately -5.5 GPa, the *Anatase* phase becomes more stable than the *Rutile* phase. With the pressure further increasing and even up to 50 GPa, the enthalpy of the new phases is still higher than that of the cubic phase, suggesting that they are metastable phases at high-pressure. Moreover, the enthalpy values of the $P6_3/mmc$ and $P6M2$ phases are almost equal within the pressure range studied. For comparison, the

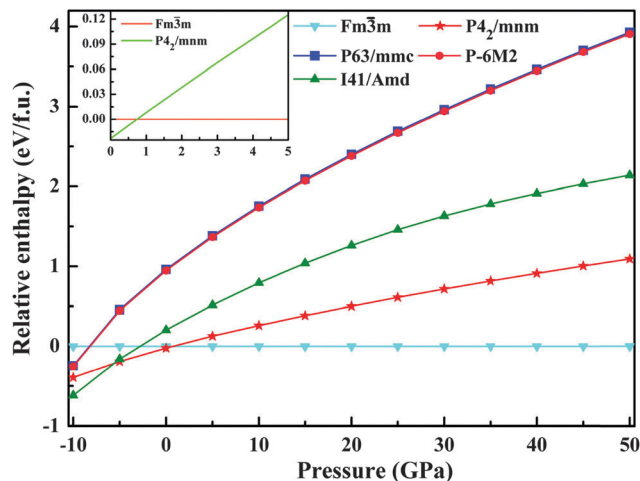


Fig. 5 The GGA-PBE calculated enthalpy curves (relative to the $Fm\bar{3}m$ phase) as a function of pressure for different Mg_2C polymorphs.

results obtained using LDA and PBESol methods are shown in Fig. S6 and S7 (ESI[†]), it is found that they are in qualitative agreement with results of the GGA-PBE method.

Aside from pressure, temperature is another pivotal factor that determines the states of materials. Therefore, we explore the high temperature stabilities of these novel phases based on the Gibbs free energy calculations within Quasi Harmonic Approximation. We calculate the temperature effect on the phase transition among different Mg_2C polymorphs up to 3000 K by PBESol xc-functional, as plotted in Fig. 6. Under ambient pressure, the new phases are still not stable relative to the $Fm\bar{3}m$ phase in the studied temperature interval (see Fig. 6a). But this situation qualitatively changes at 25 GPa, where we find that the $P4_2/mnm$

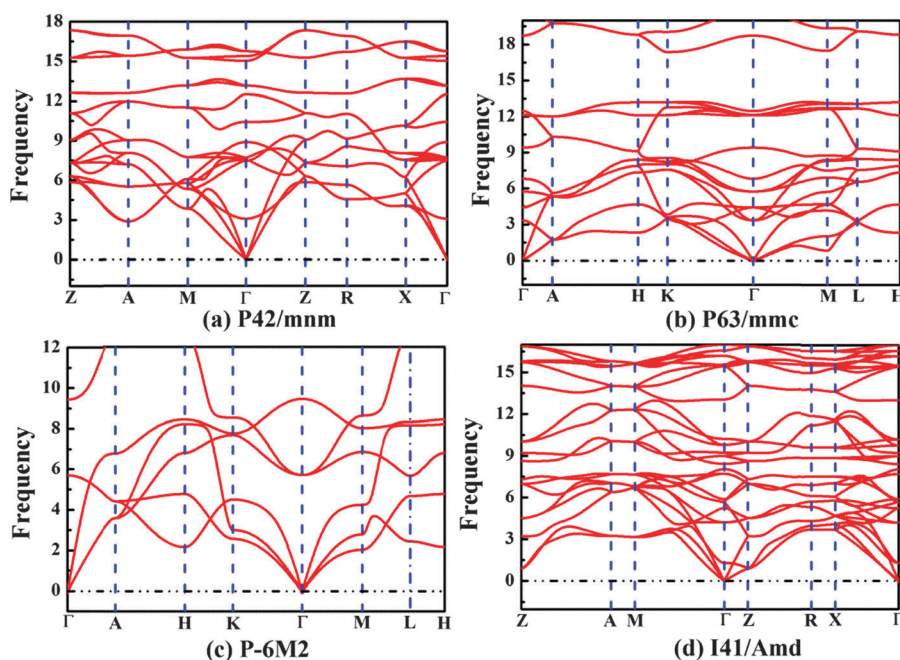


Fig. 4 Phonon dispersion curves of the newly discovered Mg_2C phases.

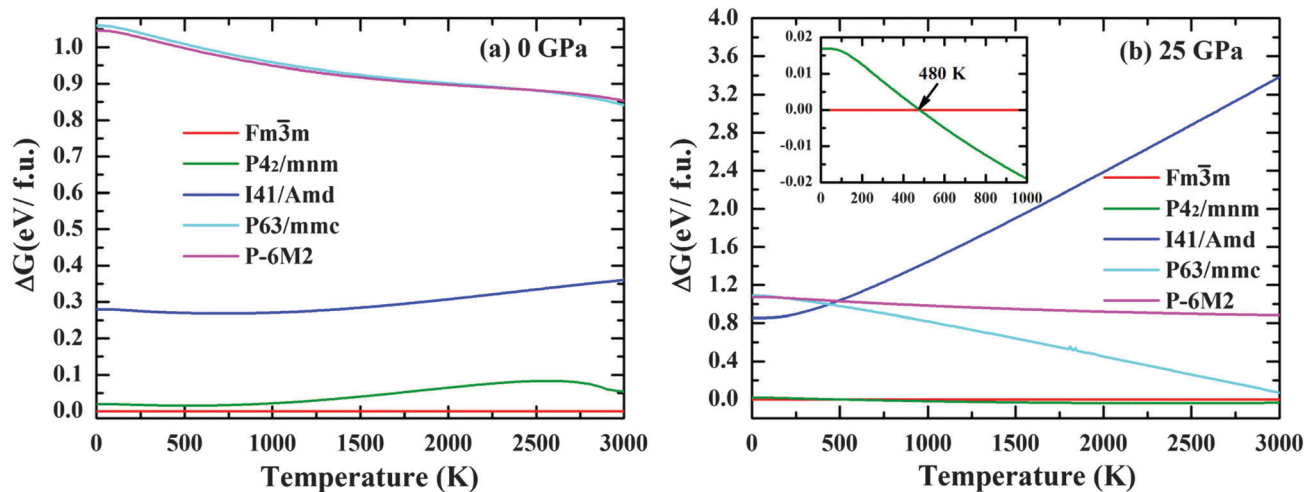


Fig. 6 The calculated energy curves as a function of temperature for the various Mg_2C polymorphs at 0 GPa and 25 GPa, respectively.

phase gets lower energy than that of the $Fm\bar{3}m$ phase at about 480 K and becomes stable, as plotted in the inset of Fig. 6(b). Moreover, the energy value of the $P\bar{6}M2$ phase is slightly higher than that of the $Fm\bar{3}m$ phase at 3000 K, indicating that temperature is also beneficial for the stabilization of the $P\bar{6}M2$ phase. Unfortunately, the other two phases remain metastable at this pressure. However, we would like to emphasize that, if one carefully controls the experimental conditions, these uncovered phases of Mg_2C may be synthesized at elevated pressure or temperature.

Incompressibility and ductility

The mechanical properties of these Mg_2C phases are investigated because they are important for applications. Fig. 7 the PBE functional calculated pressure dependence of cell volume for various Mg_2C polymorphs up to 50 GPa. It can be seen that, at zero temperature, the value of the volume decreases with increasing pressure for all structures. However, the volume decreasing extent when pressure increasing is different depends on different structure types. Comparatively, the rate of the volume reduction for the $I4_1/Amd$ phase (34.9% from zero to 50 GPa) is larger than those for the other phases, suggesting its poorer compressibility. In the same way, there is only about 25.9% volume shrinkage for the $Fm\bar{3}m$ phase when the pressure changes, indicating its higher compressibility, followed by the $P4_2/mnm$ phase (28.0%). Interestingly, the rate of the volume reduction for $P6_3/mmc$ and $P\bar{6}M2$ phases is equivalent (32.5%). In addition, we also calculate the pressure–volume data for the different phases of Mg_2C using the LDA and PBEsol methods, their results are comparable to that of PBE, which are plotted in Fig. S1 and S2 (ESI†).

On the basis of the Voigt–Reuss–Hill approximation,³⁸ the corresponding bulk and shear modulus (B and G) are obtained from the calculated elastic constants at ambient pressure. The values of B , G and B/G are also illustrated in Table 2. It is known that the bulk modulus and shear modulus can reflect the hardness of solid. The bulk modulus is the relationship of resistance with respect to volume change under certain pressure,

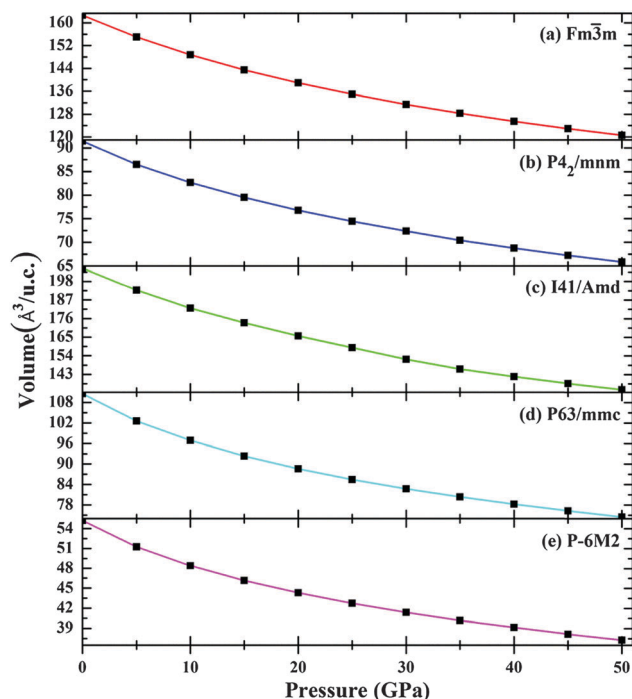


Fig. 7 The PBE functional calculated pressure dependence of cell volume for various Mg_2C polymorphs.

whereas the shear modulus is the relationship between the resistance to reversible deformations and the shear stress.³⁹ Therefore, shear modulus can supply better characterization of the mechanical properties. The calculated shear modulus for the $Fm\bar{3}m$ phase (75.2 GPa) is higher than the others, which indicates that it can withstand higher shear stress than other structures, followed by the $P4_2/mnm$ phase. In contrast, the $P\bar{6}M2$ phase has the lowest shear modulus. According to Pugh's criterion,⁴⁰ the ratio value of B/G is commonly used to describe the ductility or brittleness of materials with 1.75 as the critical value. A material can be described as brittle (ductile) if the B/G

ratio is less (more) than 1.75. In terms of the calculated results from Table 2, the B/G value of the $I4_1/Amd$, $P6_3/mmc$ and $P\bar{6}M2$ phase exceeds the critical value and implies their ductile nature. The ductility of the $Fm\bar{3}m$ ($B/G = 1.18$) and $P4_2/mnm$ phase is less than that of the above mentioned three phases.

Electronic properties

Fig. 8 shows the GGA-PBE calculated band structures and density of states (DOS) of four new phases of Mg_2C along the selected high symmetry directions of the first Brillouin zone at ambient pressure. The $P4_2/mnm$, $P6_3/mmc$ and $P\bar{6}M2$ phases exhibit obvious metallic character, with the valence band and conduction band crossing the Fermi level, as shown in Fig. 8(a), (c) and (d). While the band structure of the $I4_1/Amd$ phase (Fig. 8(b)) shows semimetallic properties, with a slight overlap between the first conduction band and the last valence band. However, it is noteworthy that the previously proposed magnesium carbides are all nonmetallic with the band gaps of 3.0 eV (MgC_2),⁵ 2.09 eV (α - Mg_2C_3),¹¹ 2.52 eV (β - Mg_2C_3)¹¹ and 0.973 eV (cubic Mg_2C).¹² Therefore, these new Mg_2C phases are quite meaningful for the Mg–C system.

In Fig. 8 we also present a detailed calculation of total and partial densities of states, DOS, where we show the contributions of each atomic orbital for each band. All these phases possess finite $N(E_F)$ at the Fermi level. Hence, they are said to exhibit certain metallicity in their crystalline state. The typical

feature of the total electronic DOS for these phases is the presence of the so-called “pseudogap” (a sharp valley around the Fermi energy), a borderline between the bonding and antibonding orbital.⁴¹ Moreover, the total DOS of the Fermi level for the $P4_2/mnm$ and $I4_1/Amd$ phases is significantly smaller than that of the $P6_3/mmc$ and $P\bar{6}M2$ phases, indicating that the $P6_3/mmc$ and $P\bar{6}M2$ phases may have more conducting electrons at the Fermi level than the other two phases. Below and above the Fermi level, each orbital of Mg and C atoms shows some extent of hybridization. However, near the Fermi level, the C 2p orbital dominates the conduction properties, whereas the Mg atoms contribute little.

It is well known that the DFT-GGA calculations generally underestimate the band gap for semiconductors and insulators (in most cases just 50–80% of the experimentally obtained band gap). To examine the validity of the GGA-PBE when treating the band structures of these new phases, the LDA and PBEsol xc-functionals are also adopted to double confirm our results, as plotted in Fig. S3 and S4 (ESI[†]). Excellent mutual agreement among the different xc-functionals supports the rationality of the current results.

Charge density distributions serve as a complementary tool and can provide a proper understanding of the electronic structure and bonding features of the system. Thus we calculate the electron density for each new phase to clarify the nature of the bonding between these two elements of Mg_2C . Fig. 9 exhibits

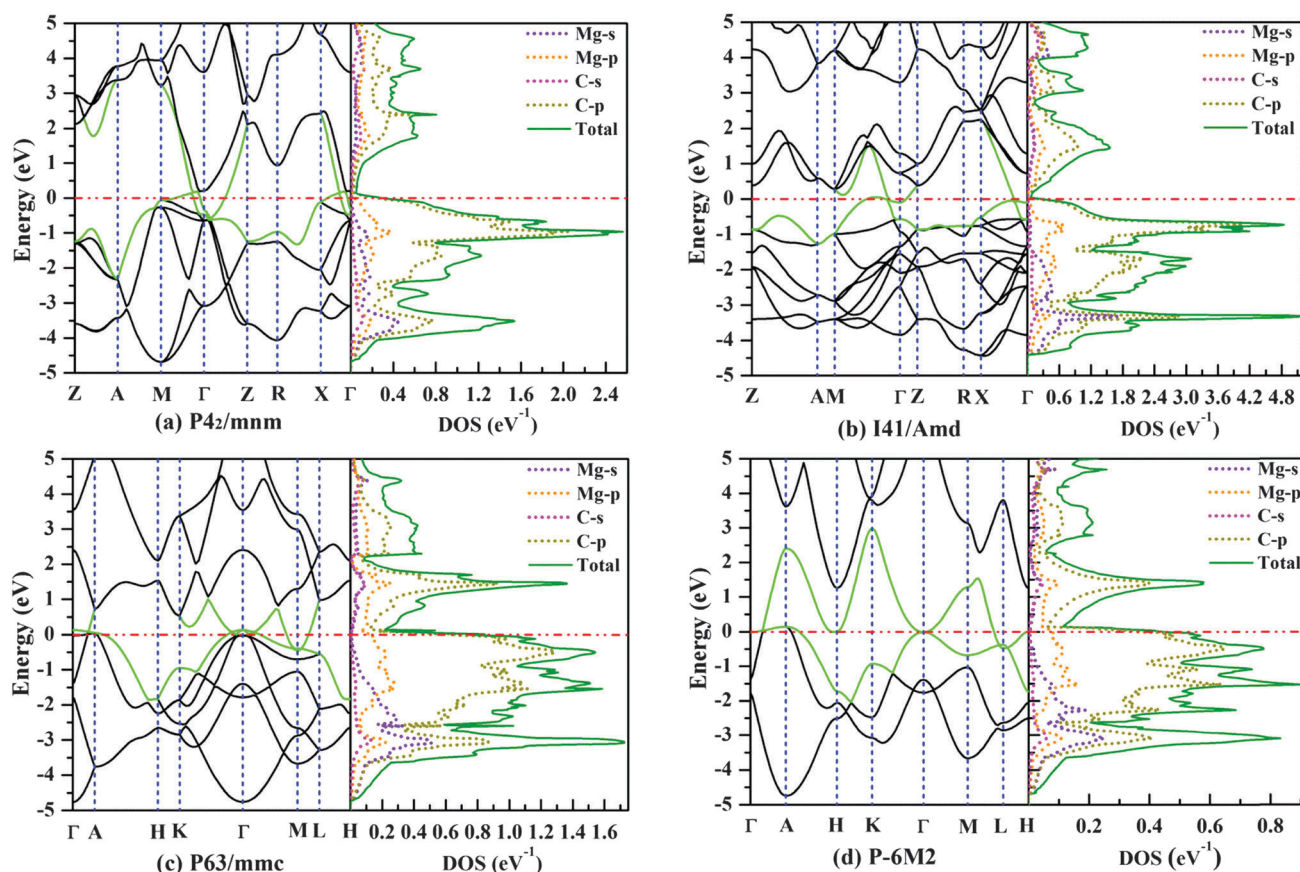


Fig. 8 Calculated band structure (left panel) and electronic DOS plots (right panel) for the newly proposed phases at ambient pressure.

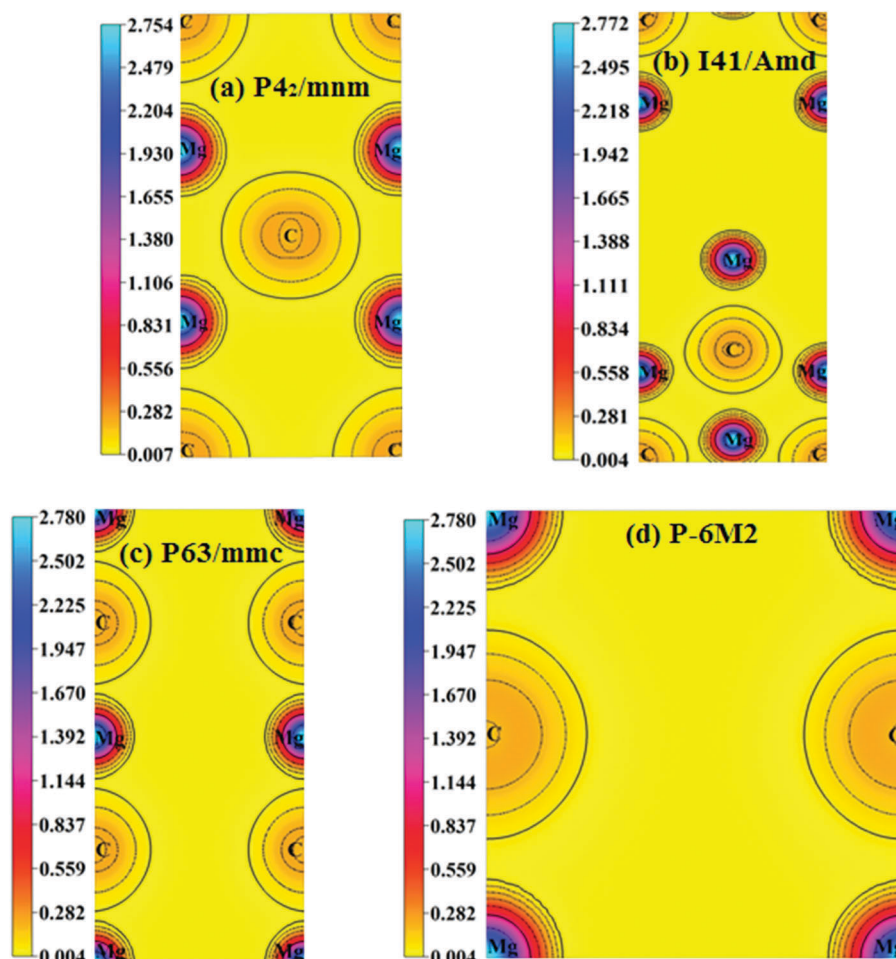


Fig. 9 The charge-density distribution maps for the selected slices of (a) $P4_2/mnm$, (b) $I4_1/Amd$, (c) $P6_3/mmc$ and (d) $P\bar{6}M2$.

the calculated charge density distribution of $P4_2/mnm$ along the (-110) plane and the others along the (100) plane. From Fig. 9(a)–(d), there are some electrons gather around the Mg atoms, whereas almost no electrons distribution around the C atoms, which suggest significant charge transfer from C to Mg atoms and a ionic feature of bonding between Mg and C atoms in these new phases. In terms of the ionic bonding character of Mg–C bonds, these novel Mg_2C phases are similar to the known $Fm\bar{3}m$ phase.¹³

Conclusions

In conclusion, we have extensively explored the potential crystal structures of stoichiometric Mg_2C by *ab initio* evolutionary crystal structure prediction. Indeed, we uncovered four intriguing phases: $P4_2/mnm$, $I4_1/Amd$, $P6_3/mmc$ and $P\bar{6}M2$. The calculated elastic constants and phonon dispersion curves suggest that all these phases are mechanical and dynamical stable. On the basis of different first-principles calculation methods, it is found that the enthalpy of the $P4_2/mnm$ phase is very close to that of the known $Fm\bar{3}m$ phase at lower pressure. We also calculate the temperature effect on the phase transition among

different Mg_2C polymorphs up to 3000 K. It is found that the $P4_2/mnm$ phase gets lower energy and becomes stable at about 480 K. Moreover, the calculated B/G ratios indicate that the $I4_1/Amd$, $P6_3/mmc$ and $P\bar{6}M2$ phases behave in a ductile manner, whereas the $P4_2/mnm$ phase exhibits brittle characteristics as well as the $Fm\bar{3}m$ phase does. In addition, the calculated band structures and PDOS results demonstrate that the $I4_1/Amd$ phase is semimetallic, while the other new phases are all metallic, which is different from the previously proposed magnesium carbides. The charge density distribution map suggests an ionic bonding feature between Mg and C atoms in these new phases. We hope that these calculations will stimulate extensive experimental work on these technologically important Mg_2C phases.

Acknowledgements

This work was supported by the Research Foundation of Education Bureau of Hebei Province (ZD20131039), the Natural Science Foundation of Hebei Province (E2014203243) and the NSFC (Grant No. 51121061), which is gratefully acknowledged.

References

- 1 M. Atoji and R. C. Medrud, *J. Chem. Phys.*, 1959, **31**, 332–337.
- 2 O. Reckeweg, A. Baumann, H. A. Mayer, J. Glaser and H. J. Meyer, *Z. Anorg. Allg. Chem.*, 1999, **625**, 1686–1692.
- 3 U. Ruschewitz, *Coord. Chem. Rev.*, 2003, **244**, 115–136.
- 4 A. Largo, P. Redondo and C. Barrientos, *J. Am. Chem. Soc.*, 2004, **126**, 14611–14619.
- 5 P. Srepusharawoot, A. Blornqvist, C. M. Araújo, R. H. Scheicher and R. Ahuja, *Phys. Rev. B: Condens. Matter Mater. Phys.*, 2010, **82**, 125439.
- 6 A. J. Karttunen, T. F. Fässler, M. Linnolahti and T. A. Pakkanen, *Inorg. Chem.*, 2011, **50**, 1733–1742.
- 7 S. Yamanaka, *Dalton Trans.*, 2010, **39**, 1901–1915.
- 8 P. Karen, A. Kjekshus, Q. Huang and V. L. Karen, *J. Alloys Compd.*, 1999, **282**, 72–75.
- 9 J. Z. Novák, *Phys. Chem.*, 1910, **73**, 513.
- 10 H. Fjellvag and P. Karen, *Inorg. Chem.*, 1992, **31**, 3260–3263.
- 11 T. A. Strobel, O. O. Kurakevych, D. Y. Kim, Y. L. Godec, W. Crichton, J. Guignard, N. Guignot, G. D. Cody and A. R. Oganov, *Inorg. Chem.*, 2014, **53**, 7020–7027.
- 12 J. L. Corkill and M. L. Cohen, *Phys. Rev. B: Condens. Matter Mater. Phys.*, 1993, **48**, 17138–17144.
- 13 O. O. Kurakevych, T. A. Strobel, D. Y. Kim and G. D. Cody, *Angew. Chem.*, 2013, **125**, 9098–9101.
- 14 O. O. Kurakevych and Y. L. Godec, *J. Phys. Chem. C*, 2014, **118**, 8128–8133.
- 15 F. Kalarasse and B. Bennecer, *J. Phys. Chem. Solids*, 2008, **69**, 1775–1781.
- 16 S. Laref and A. Laref, *Comput. Mater. Sci.*, 2008, **44**, 664–669.
- 17 T. Li, W. Ju, H. Liu, H. Cui, X. Zhao, Y. Yong and Z. Feng, *Comput. Mater. Sci.*, 2014, **93**, 234–238.
- 18 J. C. Schön and M. Jansen, *Int. J. Mater. Res.*, 2009, **100**, 135–152.
- 19 S. M. Woodley and R. Catlow, *Nat. Mater.*, 2008, **7**, 937–946.
- 20 C. J. Pickard and R. J. Needs, *J. Phys.: Condens. Matter*, 2011, **23**, 053201.
- 21 A. R. Oganov and C. W. Glass, *J. Chem. Phys.*, 2006, **124**, 244704.
- 22 A. R. Oganov, A. O. Lyakhov and M. Valle, *Acc. Chem. Res.*, 2011, **44**, 227–237.
- 23 A. O. Lyakhov, A. R. Oganov, H. T. Stokes and Q. Zhu, *Comput. Phys. Commun.*, 2013, **184**, 1172–1182.
- 24 G. Kresse and J. Furthmüller, *Phys. Rev. B: Condens. Matter Mater. Phys.*, 1996, **54**, 11169–11186.
- 25 P. E. Blöchl, *Phys. Rev. B: Condens. Matter Mater. Phys.*, 1994, **50**, 17953–17979.
- 26 R. G. Parr, *Annu. Rev. Phys. Chem.*, 1983, **34**, 631–656.
- 27 J. P. Perdew, K. Burke and M. Ernzerhof, *Phys. Rev. Lett.*, 1996, **77**, 3865–3868.
- 28 G. Kresse and D. Joubert, *Phys. Rev. B: Condens. Matter Mater. Phys.*, 1999, **59**, 1758–1775.
- 29 D. M. Ceperley and B. J. Alder, *Phys. Rev. Lett.*, 1980, **45**, 566–569.
- 30 J. P. Perdew and A. Zunger, *Phys. Rev. B: Condens. Matter Mater. Phys.*, 1981, **23**, 5048–5079.
- 31 J. P. Perdew, A. Ruzsinszky, G. I. Csonka, O. A. Vydrov, G. E. Scuseria, L. A. Constantin, X. L. Zhou and K. Burke, *Phys. Rev. Lett.*, 2008, **100**, 136406.
- 32 H. J. Monkhorst and J. D. Pack, *Phys. Rev. B: Solid State*, 1976, **13**, 5188–5192.
- 33 A. Togo, F. Oba and I. Tanaka, *Phys. Rev. B: Condens. Matter Mater. Phys.*, 2008, **78**, 134106.
- 34 M. D. Segall, P. J. D. Lindan, M. J. Probert, C. J. Pickard, P. J. Hasnip, S. J. Clark and M. C. Payne, *J. Phys.: Condens. Matter*, 2002, **14**, 2717–2744.
- 35 F. Mouhat and F.-X. Coudert, *Phys. Rev. B: Condens. Matter Mater. Phys.*, 2014, **90**, 224104.
- 36 M. A. Zwijnenburg, K. E. Jelfs and S. T. Bromley, *Phys. Chem. Chem. Phys.*, 2010, **12**, 8505–8512.
- 37 M. A. Zwijnenburg and S. T. Bromley, *Phys. Rev. B: Condens. Matter Mater. Phys.*, 2011, **83**, 024104.
- 38 R. Hill, *Proc. Phys. Soc., London, Sect. A*, 1952, **65**, 349–354.
- 39 A. F. Young, C. Sanloup, E. Gregoryanz, S. Scandolo, R. J. Hemley and H. Mao, *Phys. Rev. Lett.*, 2006, **96**, 155501.
- 40 S. F. Pugh, *Philos. Mag.*, 1954, **7**, 823–843.
- 41 P. Vajeeston, P. Ravindran, C. Ravi and R. Asokamani, *Phys. Rev. B: Condens. Matter Mater. Phys.*, 2001, **63**, 045115.